

Bispectral mode decomposition of nonlinear flows

Oliver T. Schmidt^{1†}

¹Department of Mechanical and Aerospace Engineering, University of California San Diego, La Jolla, CA, USA

(Received xx; revised xx; accepted xx)

Triadic interactions are the fundamental mechanism of energy transfer in fluid flows. This work introduces bispectral mode decomposition as a direct means of educing flow structures that are associated with triadic interactions from experimental or numerical data. Triadic interactions are characterized by quadratic phase coupling which can be detected by the bispectrum. The proposed method maximizes an integral measure of this third-order statistic to compute modes associated with frequency triads, as well as a mode bispectrum that identifies resonant three-wave interactions. Based on these two main outcomes, two additional derived quantities are defined: interaction maps that indicate regions of nonlinear coupling, and the summed mode bispectrum as a compact representation of the mode bispectrum. Different aspects of the decomposition are demonstrated on direct numerical simulation data of laminar cylinder flow at $Re = 500$, particle image velocimetry data of massively-separated flow behind flat plate at high angle of attack, and large eddy simulation data of a transitional round jet at $Re = 3600$.

Key words:

1. Introduction

Triadic interactions result from the quadratic nonlinearity of the Navier-Stokes equations. They are the fundamental mechanism of energy transfer in fluid flows and manifest, in Fourier space, as triplets of three wavenumber vectors, $\{\mathbf{k}_j, \mathbf{k}_k, \mathbf{k}_l\}$, or frequencies, $\{f_j, f_k, f_l\}$, that sum to zero:

$$\mathbf{k}_j \pm \mathbf{k}_k \pm \mathbf{k}_l = \mathbf{0}, \quad f_j \pm f_k \pm f_l = 0. \quad (1.1)$$

For clarity, we denote by $\{\cdot\}$ frequency and by (\cdot) index multiplate, respectively.

The zero-sum condition implies that triads form triangles in wavenumber- and frequency-space. Since the early work of Phillips (1960) on weak resonant interactions of gravity waves on the surface of deep water, interaction theory has vastly improved our understanding of nonlinear wave phenomena. The turbulent cascade, which describes the transfer of energy from large to small scales of motion, is probably the most prominent consequence of triadic interactions. Following the seminal work by Kraichnan (1967, 1971), the role of triad interactions and triad truncation in homogenous turbulence has been studied by numerous authors including Waleffe (1992) and Moffatt (2014), among many others. Triads play a similarly important role in the laminar-turbulent transion process. This was demonstrated by Craik (1971), who showed that resonant

† Email address for correspondence: oschmidt@ucsd.edu

triads of Tollmien-Schlichting waves provide an efficient mechanism for rapid transition in wall-bounded shear flows.

Because of their ubiquitous role turbulent and transitional flows, it comes as no surprise that triad interaction play an important role in reduced-order modeling. The class of models with dynamics that are restricted to triadic interactions that involve the mean flow, for example, is referred to as quasilinear models. Recent examples that use this specific type of triad truncation include the statistical state dynamics model by Farrell & Ioannou (2003) and the restricted nonlinear approximation by Thomas *et al.* (2014); Farrell *et al.* (2016). Rather than formally decomposing the flow into mean and fluctuations, the generalized quasilinear approximation by Marston *et al.* (2016) uses a spectral filter to separate different scales of motion. A modeling approach based on linear input-output dynamics is summarized in McKeon (2017). We refer to the latter reference for a comprehensive overview of scale interactions in wall turbulence with emphasis on triad interactions. In the context of computational fluid mechanics, triad truncation can be understood as the wave-space manifestation of the turbulence closure problem. Large eddy simulation, for example, refers to the solution of the low-pass filtered Navier-Stokes equations and requires closure of the subgrid scale stress tensor. If large eddy simulation is conducted in wavenumber space, the closure problem explicitly becomes that of modeling the effect of all triads that are effected by wavenumber cutoff on the resolved larger scales (see, e.g., Pope 2000).

Higher-order statistical analysis refers to signal processing of time-series using higher-order spectra, or polyspectra. Of primary interest in the context of triadic interactions in self-excited and forced fluid flows is the bispectrum. Just like the power spectrum, the bispectrum can be estimated by ensemble-averaging products of realizations of the Fourier transform (Kim & Powers 1979). Unlike the power spectrum, which is real-valued by construction and carries no phase information, the bispectrum is capable of detecting quadratic phase-coupling by correlating different wave components. theoretical form of the bispectrum for Kraichnan's statistical models of homogenous turbulence has been devised and validated by Herring (1980); Herring & Métais (1992). Using the bispectrum, Corke & Mangano (1989) experimentally investigated the triadic interaction of phase-coupled input disturbances to a laminar boundary layer. Later, Corke *et al.* (1991) studied the mode selection process and resonant phase locking in forced axisymmetric jets using the bispectrum. Other experimental studies that leverage the bispectrum to investigate triadic interactions and other nonlinear phenomena include the works of Gee *et al.* (2010) on the propagation of noise from a supersonic jet, Yamada *et al.* (2010) on turbulence in plasmas, and Craig *et al.* (2019) on second-mode instability in a hypersonic boundary layer.

As large flow data of high temporal and spatial resolution have become ubiquitous, modal decomposition techniques are often applied as the primary means of flow analysis and data reduction. In fluid mechanics, the eigendecomposition of the covariance matrix is referred to as proper orthogonal decomposition (POD, Lumley 1970). The resulting modes are orthonormal and optimally represent the data in terms of its variance. Classical space-only POD based on the spatial covariance matrix (Sirovich 1987) is particularly well suited for low-order modeling (Deane *et al.* 1991; Noack *et al.* 2003), whereas frequency-domain, or spectral proper orthogonal decomposition (SPOD) is ideally suited to analyze statistically stationary data (Towne *et al.* 2018; Schmidt & Colonius 2020). Dynamic mode decomposition (DMD, Schmid 2010) permits analysis and modeling of flows in terms of the approximate eigendecomposition of the hypothetical evolution operator that maps the flow state from one snapshots to the next (see also Rowley *et al.* 2009).

Both POD and DMD are generally applicable to linear and nonlinear flow data, but

neither method explicitly accounts for nonlinear interactions. The bispectrum, on the other hand, detects quadratic nonlinear interactions, but is only applicable to time-signals. To overcome these limitations in the context of stochastic estimation, Baars *et al.* (2010) serially combined higher-order statistical analysis and modal decomposition by computing the cross-bispectrum between SPOD expansion coefficients from spatially separated, synchronized microphone arrays.

In this work, bispectral mode decomposition is introduced as a direct means of computing modes that are associated with triadic interactions. The paper is organized as follows. We discuss higher-order spectra of time-series in §2.1. theory of resonant triad interaction in laminar and turbulent flows is outlined in §2.2. In §3, bispectral mode decomposition is introduced, and some important symmetry properties are discussed in §3.1. To demonstrate the method, we analyze direct numerical simulation data of laminar cylinder flow at $Re = 500$ in §4.1, particle image velocimetry data of turbulent flow over a flat plate at high angle of attack in §4.2, and large eddy simulation data of a transitional jet at $Re = 3600$ in §4.3. A brief summary and outlook are given in §5. Appendix A gives the details of the numerical algorithm.

2. Background

2.1. Higher-order spectra

We start by introducing the concept of the bispectrum for a stationary random signal $q(t)$ with zero mean,

$$R_q = E[q(t)] = 0, \quad (2.1)$$

where $E[\cdot]$ is the expectation operator and

$$R_{q\dots q} = E[q(t)q(t - \tau_1)q(t - \tau_2)\dots q(t - \tau_{n-1})] \quad (2.2)$$

represents the n th-order moment of a stationary random signal. Through the introduction of the Fourier transform pair,

$$\hat{q}(f) = \int_{-\infty}^{\infty} q(t)e^{-i2\pi ft} dt, \quad (2.3)$$

$$q(t) = \int_{-\infty}^{\infty} \hat{q}(f)e^{i2\pi ft} df, \quad (2.4)$$

we can relate the signals power, or variance,

$$E[q(t)^2] = \int_{-\infty}^{\infty} S_{qq}(f) df \quad (2.5)$$

to the power spectral density, or power spectrum,

$$S_{qq}(f) = \lim_{T \rightarrow \infty} \frac{1}{T} E[\hat{q}(f)\hat{q}(f)^*]. \quad (2.6)$$

Note that the power spectrum is real, and therefore phase blind. It is directly related to the second-order moment, that is the autocorrelation function $R_{qq}(\tau) = E[q(t), q(t - \tau)]$ via the Fourier transform,

$$S_{qq}(f) = \int_{-\infty}^{\infty} R_{qq}(\tau)e^{-i2\pi f\tau} d\tau. \quad (2.7)$$

This is the well-known Wiener-Khinchine theorem. Analogously, the bispectrum, or bispectral density, is defined as the double Fourier transform of the third moment,

$$S_{qqq}(f_1, f_2) = \int_{-\infty}^{\infty} \int_{-\infty}^{\infty} R_{qqq}(\tau_1, \tau_2) e^{-i2\pi(f_1\tau_1 + f_2\tau_2)} d\tau_1 d\tau_2, \quad (2.8)$$

and is a function of two frequencies, f_1 and f_2 . Integration over the bispectrum recovers the expected value of the cubed signal, or skewness,

$$E[q(t)^3] = \int_{-\infty}^{\infty} \int_{-\infty}^{\infty} S_{qqq}(f_1, f_2) df_1 df_2. \quad (2.9)$$

Hence, the bispectrum decomposes the skewness of a stationary random signal into its frequency components. Since the skewness of symmetric distributions such as the Gaussian distribution is zero, the bispectrum is a direct measure of non-Gaussianity. Most important in the context of three-wave interactions, as discussed in §2.2 below, is the observation that the bispectrum correlates two frequency components to their sum. This can readily be seen from its definition in terms of the expectation operator,

$$S_{qqq}(f_1, f_2) = \lim_{T \rightarrow \infty} \frac{1}{T} E[\hat{q}(f_1)^* \hat{q}(f_2)^* \hat{q}(f_1 + f_2)], \quad (2.10)$$

or, alternatively,

$$S_{qqq}(f_1, f_2) = \lim_{T \rightarrow \infty} \frac{1}{T} E[\hat{q}(f_1) \hat{q}(f_2) \hat{q}(f_1 + f_2)^*]. \quad (2.11)$$

Equation (2.10) is consistent with definition (2.2) of the n th-order moment in terms of time delays τ , whereas equation (2.11) is associated with the interpretation of τ as time advances.

For further details on bi- and higher-order spectra, such as the definition of the bicoherence as a common normalization of the bispectrum, the reader is referred to the reviews by Collis *et al.* (1998); Brillinger (1965); Kim & Powers (1979); Nikias & Raghunath (1987); Nikias & Mendel (1993). In §3.1, we will discuss the symmetry properties which bispectral mode decomposition inherits from the bispectrum.

2.2. Triad interaction and resonance conditions

Triad interaction is a specific type of three-wave coupling that results from quadratic nonlinearities in the governing equations. Assume the dynamics of the state $\mathbf{q} = \mathbf{q}(\mathbf{x}, t)$ are governed by an evolution equation of the form

$$\frac{\partial \mathbf{q}}{\partial t} = \mathcal{L}\mathbf{q} + \mathcal{Q}(\mathbf{q}, \mathbf{q}), \quad (2.12)$$

where $\mathbf{x} = [x, y, z]^T$ is the position vector, \mathcal{L} a linear operator and $\mathcal{Q}(\cdot, \cdot)$ a quadratic (bilinear) nonlinearity. In the context of fluid flows governed by the incompressible Navier-Stokes equations (NSE), the convective term $(\mathbf{u} \cdot \nabla)\mathbf{u}$ represents such a quadratic nonlinearity. $\mathbf{u} = [u, v, w]^T$ is the Cartesian velocity vector. We further assume that there exists an equilibrium solution $\mathbf{q}_0 = \mathbf{q}_0(\mathbf{x})$ of equation (2.12) such that

$$\mathcal{L}\mathbf{q}_0 + \mathcal{Q}(\mathbf{q}_0, \mathbf{q}_0) = 0, \quad (2.13)$$

i.e., a stable, steady, laminar flow that is a solution of the NSE. Next, we decompose solutions to equation (2.12) into small but finite fluctuations around the equilibrium \mathbf{q}_0 in the form of a series

$$\mathbf{q}(\mathbf{x}, t) = \mathbf{q}_0(\mathbf{x}) + \epsilon \mathbf{q}'(\mathbf{x}, t) + \epsilon^2 \mathbf{q}''(\mathbf{x}, t) + \dots \quad \text{with} \quad 0 < \epsilon \ll 1, \quad (2.14)$$

of powers of ϵ . Inserting equations (2.13) and (2.14) into equation (2.12), yields at leading order $\mathcal{O}(\epsilon)$ the equation

$$\frac{\partial \mathbf{q}'}{\partial t} = \mathcal{L} \mathbf{q}'. \quad (2.15)$$

Due to linearity, periodic solutions to equation (2.28) take the form

$$\mathbf{q}'(\mathbf{x}, t) \propto e^{i(\mathbf{k} \cdot \mathbf{x} - 2\pi f t)}. \quad (2.16)$$

Combining equations (2.16) and (2.15) yield the dispersion relation

$$f = D(\mathbf{k}) \quad (2.17)$$

for the linear problem which relates frequency and the wavenumber vector. Suppose equation (2.15) possesses N periodic solutions

$$\mathbf{q}'_n(\mathbf{x}, t) = A_n e^{i(\mathbf{k}_n \cdot \mathbf{x} - 2\pi f_n t)} + \text{c.c.}, \quad (2.18)$$

where $A = A(\mathbf{k}, f)$ is a complex amplitude and c.c. symbolizes the complex conjugate, $A^* e^{-i(\mathbf{k} \cdot \mathbf{x} - 2\pi f t)}$. For brevity, we introduce as

$$\theta_n \equiv \mathbf{k}_n \cdot \mathbf{x} - 2\pi f_n t \quad (2.19)$$

the phase function. Also due to linearity, any sum of solutions \mathbf{q}'_n also solves equation (2.15). We may hence express the general solution as

$$\mathbf{q}'(\mathbf{x}, t) = \sum_{n=1}^N (A_n e^{i\theta_n} + \text{c.c.}). \quad (2.20)$$

At $\mathcal{O}(\epsilon^2)$, we obtain the evolution equation obeyed by \mathbf{q}'' ,

$$\frac{\partial \mathbf{q}''}{\partial t} = \mathcal{L} \mathbf{q}'' + \mathcal{Q}(\mathbf{q}', \mathbf{q}'). \quad (2.21)$$

In this equation, the nonlinearity first manifests in the form of the weakly nonlinear interaction of the linear solution \mathbf{q}' with itself. Expanding the nonlinear term yields

$$\begin{aligned} \mathcal{Q}(\mathbf{q}', \mathbf{q}') &= \sum_{n=1}^N (A_n e^{i\theta_n} + \text{c.c.}) \sum_{m=1}^N (A_m e^{i\theta_m} + \text{c.c.}) \\ &= 2A_1 A_1^* + A_1^2 e^{i2\theta_1} + A_1^{*2} e^{-i2\theta_1} + A_1 A_2 e^{i(\theta_1 + \theta_2)} \\ &\quad + A_1 A_2^* e^{i(\theta_1 - \theta_2)} + A_1^* A_2 e^{i(-\theta_1 + \theta_2)} + A_1^* A_2^* e^{i(-\theta_1 - \theta_2)} \\ &\quad + \dots \end{aligned} \quad (2.22)$$

The first three terms of this sum result from the self-interaction of \mathbf{q}'_1 . The first term has zero frequency and therefore contributes to the mean flow deformation. The second and third terms contribute to the first harmonic of \mathbf{q}'_1 which oscillates at $2f_1$. The fourth and fifth term are the sum and difference interactions of \mathbf{q}'_1 and \mathbf{q}'_2 . Their respective phases are given as the sums and differences of their individual phases. In a slight change of notation for the subindices, denote by $\theta_j \equiv \theta_k \pm \theta_l$, or equivalently by

$$f_j \equiv f_k \pm f_l, \quad (2.23a)$$

$$\mathbf{k}_j \equiv \mathbf{k}_k \pm \mathbf{k}_l, \quad (2.23b)$$

the sums and differences of any two wave components, $\theta_k = \mathbf{k}_k \cdot \mathbf{x} - 2\pi f_k t$ and $\theta_l = \mathbf{k}_l \cdot \mathbf{x} - 2\pi f_l t$, generated by quadratic interaction. Equations (2.23a,b) are equivalent to

equation (1.1). Now assume one of these newly generated wave components satisfies the dispersion relation for the linear system (2.17), that is,

$$f_j = D(\mathbf{k}_j). \quad (2.24)$$

This has two important implications. First, the $\{f_j, \mathbf{k}_j\}$ component satisfies the linear portion of equation (2.21). Second, the linear portion of equation (2.21) is resonantly forced by the $\mathcal{O}(\epsilon^2)$ products in equation (2.22) that share the same frequency and wavenumber. As a result, the corresponding wave component grows linearly in time and the system is said to be in resonance. Under these circumstances, equations (2.23a) and (2.23b) establish a quadratic coupling of the phases between the k , l and $k+l$ wave components. We refer to these frequency triplets $\{f_k, f_l, f_{k+l}\}$ or frequency index triplets $(k, l, k+l)$ as resonant (frequency) triads. Conversely, correlation between two wave components and their sum indicates the presence of a quadratic nonlinearity. For time signals, this property is exploited by the bispectrum, as can be seen from its definition, equation (2.10). The amplitude equations that govern the saturation of resonant waves are discussed in standard texts like Craik (1988) or Schmid & Henningson (2001).

For turbulent flows, equation (2.12), in general, does not possess a stable equilibrium solution \mathbf{q}_0 . In this case, instead of fluctuations about an equilibrium, we may consider fluctuations \mathbf{q}' around the mean flow

$$\bar{\mathbf{q}}(\mathbf{x}) = \frac{1}{T} \int_0^T \mathbf{q}(\mathbf{x}, t) dt. \quad (2.25)$$

Inserting the (Reynolds) decomposition

$$\mathbf{q}(\mathbf{x}, t) = \bar{\mathbf{q}}(\mathbf{x}) + \mathbf{q}'(\mathbf{x}, t) \quad (2.26)$$

into equation (2.12) and averaging over time yields the mean flow equation,

$$\mathbf{0} = \mathcal{L}\bar{\mathbf{q}} + \mathcal{Q}(\bar{\mathbf{q}}, \bar{\mathbf{q}}) + \overline{\mathcal{Q}(\mathbf{q}', \mathbf{q}')}, \quad (2.27)$$

where we used the property $\frac{\partial \bar{\mathbf{q}}}{\partial t} = \overline{\frac{\partial \mathbf{q}'}{\partial t}} = 0$. These are the Reynolds-averaged Navier-Stokes (RANS) equations and $\mathcal{Q}(\mathbf{q}', \mathbf{q}')$ are the Reynolds stresses. Linearizing about the mean flow and using equation (2.27) yields the equations obeyed by the fluctuations,

$$\frac{\partial \mathbf{q}'}{\partial t} = \mathcal{L}_{\bar{\mathbf{q}}} \mathbf{q}' - \overline{\mathcal{Q}(\mathbf{q}', \mathbf{q}')}, \quad (2.28)$$

where

$$\mathcal{L}_{\bar{\mathbf{q}}} \equiv \mathcal{L} + \mathcal{Q}(\cdot, \bar{\mathbf{q}}) + \mathcal{Q}(\bar{\mathbf{q}}, \cdot) \quad (2.29)$$

defines the linearized Navier-Stokes operator with respect to linearization about the mean flow. The Reynolds stresses $\overline{\mathcal{Q}(\mathbf{q}', \mathbf{q}')}$ in equations (2.27) and (2.28) hinder the application of the resonant interaction theory presented above. To show that similar kinematic arguments apply to turbulent flows nevertheless, suppose that the fluctuating component $\mathbf{q}'(x, y, z, t)$ can be represented as a Fourier series,

$$\mathbf{q}'(x, y, z, t) = \sum_{m, n=-\infty}^{\infty} \hat{\mathbf{q}}_{mn}(x, y) e^{i(k_m z - 2\pi f_n t)}, \quad (2.30)$$

of periods T in time and L in the z -direction, where $f_n = n/T$ is frequency and $k_m = 2\pi m/L$ wavenumber. The example of a flow with one homogeneous direction, z , and two inhomogeneous directions, x and y , is chosen without loss of generality. Inserting

equation (2.30) into (2.26) yields the Reynolds decomposition of this flow,

$$\mathbf{q}(\mathbf{x}, t) = \bar{\mathbf{q}}(x, y) + \sum_{m,n} \hat{\mathbf{q}}_{mn}(x, y) e^{i\theta_{mn}}, \quad (2.31)$$

where the mean is taken over time and in the z -direction. For brevity, we denote as

$$\theta_{mn} \equiv k_m z - 2\pi f_n t \quad (2.32)$$

the phase function and omit the limits of summation in equation (2.31) and in the following. Due to the prior removal of the mean, the $(m, n) = (0, 0)$ wave component does not contribute to the Fourier sum in equation (2.33) since $\hat{\mathbf{q}}_{00}(x, y) = \mathbf{0}$. Inserting the Reynolds decomposition (2.31) into the governing nonlinear equation (2.12) yields

$$\begin{aligned} -2\pi i \sum_{m,n} f_n \hat{\mathbf{q}}_{mn} e^{i\theta_{mn}} &= \mathcal{L}\bar{\mathbf{q}} + \mathcal{Q}(\bar{\mathbf{q}}, \bar{\mathbf{q}}) + \sum_{m,n} \mathcal{L}\hat{\mathbf{q}}_{mn} e^{i\theta_{mn}} \\ &+ \sum_{m,n} [\mathcal{Q}(\bar{\mathbf{q}}, \hat{\mathbf{q}}_{mn}) + \mathcal{Q}(\hat{\mathbf{q}}_{mn}, \bar{\mathbf{q}})] e^{i\theta_{mn}} + \sum_{m,n,p,q} \mathcal{Q}(\hat{\mathbf{q}}_{mn}, \hat{\mathbf{q}}_{pq}) e^{i\theta_{m+p, n+q}}. \end{aligned} \quad (2.33)$$

The generation of a $(m+p, n+q)$ wave component is apparent from the last term. This quadratic interaction process is analogous to the process described by equation (2.22) and triads also take the form of equations (2.23a) and (2.23b). The equations for the different Fourier components can be separated by exploiting the orthogonality of the complex exponential. Integration over T and L , for example, isolates the zero-frequency and -wavenumber component,

$$\mathbf{0} = \mathcal{L}\bar{\mathbf{q}} + \mathcal{Q}(\bar{\mathbf{q}}, \bar{\mathbf{q}}) + \sum_{m,n} \mathcal{Q}(\hat{\mathbf{q}}_{mn}, \hat{\mathbf{q}}_{-m-n}). \quad (2.34)$$

The sum in equation (2.34) comprises the zero-frequency and -wavenumber contributions of the quadruple sum in (2.33). These contributions result from the interaction of fluctuating wave components, (m, n) , with their conjugate counterparts, $(-m, -n)$. Comparing equations (2.34) and (2.27) shows that this contribution corresponds to the Reynolds stresses. The equation for the (m, n) -th frequency-wavenumber component is isolated by multiplying by $e^{i\theta_{mn}}$ and integrating over T and L to obtain

$$-2\pi i f_n \hat{\mathbf{q}}_{mn} = \mathcal{L}\hat{\mathbf{q}}_{mn} + \mathcal{Q}(\bar{\mathbf{q}}, \hat{\mathbf{q}}_{mn}) + \mathcal{Q}(\hat{\mathbf{q}}_{mn}, \bar{\mathbf{q}}) + \sum_{p,q} \mathcal{Q}(\hat{\mathbf{q}}_{pq}, \hat{\mathbf{q}}_{m-p, n-q}). \quad (2.35)$$

In terms of the linear operator defined in equation (2.29), this equation reads

$$-2\pi i f_n \hat{\mathbf{q}}_{mn} = \mathcal{L}_{\bar{\mathbf{q}}} \hat{\mathbf{q}}_{mn} + \sum_{p,q} \mathcal{Q}(\hat{\mathbf{q}}_{pq}, \hat{\mathbf{q}}_{m-p, n-q}). \quad (2.36)$$

This form is similar to (2.27) and similar arguments regarding the occurrence of resonances can be made. Equation (2.35) illustrates how different wave components may contribute to the power spectral density at any given frequency, and also how contributions from different wave components to any given frequency can be identified by triple correlations of frequency components, i.e., by the bispectrum.

3. Bispectral mode decomposition (BMD)

The goal of this work is to devise a modal decomposition that reveals the presence of triadic nonlinear interactions from multidimensional data. As discussed in §§2.1 and 2.2, quadratic phase coupling is characteristic of these interactions and can be detected by

the bispectrum. To compute modes that exhibit quadratic phase coupling over extended portions of the flow field, we require the decomposition to optimally represent the data in terms of an integral measure of the bispectral density. BMD may be understood as the extension of the analysis of time signals using higher-order spectra to multidimensional datasets, or *vice versa*, as an extension of spectral proper orthogonal decomposition to higher-order spectra. In particular, consider data that is given as a series of N_t consecutive flow fields

$$\mathbf{q}(\mathbf{x}, t_j) \in \mathbb{C}^{M \times 1}, \quad j = 1, 2, \dots, N_t, \quad (3.1)$$

that are evenly spaced in time. Let $M = N_{\text{vars}} N_x N_y N_z$ be the number of spatial degrees of freedom per time instant, with N_{vars} as the number of variables in the state vector, and N_x , N_y , N_z the numbers of grid points in the Cartesian directions, respectively. The bispectral density is defined in equation (2.10) as the expected value of the product of two frequency components with their sum. As an estimator for the bispectrum we adapt Welch's method (Welch 1967), which is an asymptotically consistent spectral estimator for the power spectral density. Welch's method is based on the ergodicity hypothesis. It assumes that the time average in equation (2.6) can be estimated by an ensemble average over a number of N_{blk} realizations of the Fourier transform. The underlying assumption is that the time series $\mathbf{q}(\mathbf{x}, t_j)$ is statistically stationary. Each realization is obtained as the discrete-time Fourier transform of one of N_{blk} segments consisting of N_{FFT} snapshots. To decrease the variance of the estimate, the number of segments is inflated by allowing consecutive segments to overlap by N_{ovlp} elements. Given a total number of N_t snapshots, we obtain a number of

$$N_{\text{blk}} = \text{floor} \left(\frac{N_t - N_{\text{ovlp}}}{N_{\text{FFT}} - N_{\text{ovlp}}} \right) \quad (3.2)$$

realizations of the Fourier transform, $\hat{\mathbf{q}}^{[1]}(\mathbf{x}, f)$, $\hat{\mathbf{q}}^{[2]}(\mathbf{x}, f)$, \dots , $\hat{\mathbf{q}}^{[N_{\text{blk}}]}(\mathbf{x}, f)$. The discrete Fourier transform and its inverse are defined as

$$\hat{\mathbf{q}}(\mathbf{x}, f_k) = \sum_{j=0}^{N_{\text{FFT}}-1} \mathbf{q}(\mathbf{x}, t_{j+1}) e^{-i2\pi jk/N_{\text{FFT}}}, \quad k = 0, \dots, N_{\text{FFT}} - 1, \text{ and} \quad (3.3)$$

$$\mathbf{q}(\mathbf{x}, t_{j+1}) = \frac{1}{N_{\text{FFT}}} \sum_{k=0}^{N_{\text{FFT}}-1} \hat{\mathbf{q}}(\mathbf{x}, f_k) e^{i2\pi jk/N_{\text{FFT}}}, \quad j = 0, \dots, N_{\text{FFT}} - 1. \quad (3.4)$$

The time step Δt between consecutive snapshots determines the sampling frequency $f_s = 1/\Delta t$ and thereby the Nyquist frequency $f_N = f_s/2$. Computation of the bispectrum further requires the product of two frequency components. To compute products of Fourier coefficients of multidimensional data, we use the entry-wise, or Hadamard product defined as $(\mathbf{A} \circ \mathbf{B})_{jk} = \mathbf{A}_{jk} \mathbf{B}_{jk}$. It applies to two matrices \mathbf{A} and \mathbf{B} of the same dimensions. For brevity, we introduce the shorthands

$$\hat{\mathbf{q}}_k \equiv \hat{\mathbf{q}}(\mathbf{x}, f_k), \text{ and} \quad (3.5)$$

$$\hat{\mathbf{q}}_{k \circ l} \equiv \hat{\mathbf{q}}(\mathbf{x}, f_k) \circ \hat{\mathbf{q}}(\mathbf{x}, f_l), \quad (3.6)$$

for the k -th frequency component of the discrete-time Fourier transform and the spatial entry-wise product of two realizations of the Fourier transform at frequencies f_k and f_l , respectively. At the heart of bispectral mode decomposition is the definition of an integral measure

$$b(f_k, f_l) \equiv E \left[\int_{\Omega} \hat{\mathbf{q}}_k^* \circ \hat{\mathbf{q}}_l^* \circ \hat{\mathbf{q}}_{k+l} \, d\mathbf{x} \right] = E [\hat{\mathbf{q}}_{k \circ l}^H \mathbf{W} \hat{\mathbf{q}}_{k+l}] = E [\langle \hat{\mathbf{q}}_{k \circ l}, \hat{\mathbf{q}}_{k+l} \rangle], \quad (3.7)$$

of the point-wise bispectral density. By $(\cdot)^*$, $(\cdot)^T$, and $(\cdot)^H$ we distinguish the complex conjugate, transpose, and complex transpose, respectively. \mathbf{W} is the diagonal matrix of spatial quadrature weights and Ω the spatial domain over which the flow is defined. The weighted inner product,

$$\langle \mathbf{q}_1, \mathbf{q}_2 \rangle = \mathbf{q}_1^H \mathbf{W} \mathbf{q}_2, \quad (3.8)$$

is introduced as the discrete analogue to spatial integration. In equation (3.7), the combination of the l -th and k -th frequency components into $\hat{\mathbf{q}}_{kol}^H \equiv \hat{\mathbf{q}}_k^* \circ \hat{\mathbf{q}}_l^*$ is merely notational. In the following, however, we explicitly take into account the causal relation between the sum frequency component \hat{q}_{k+l} (effect), and the product of the l -th and k -th frequency components, $\mathcal{Q}(\hat{q}_k, \hat{q}_l) \propto \hat{q}_k \hat{q}_l$ (cause), that form a resonant triad, and define two linear expansions

$$\phi_{kol}^{[i]}(\mathbf{x}, f_k, f_l) = \sum_{j=1}^{N_{\text{blk}}} a_{ij}(f_{k+l}) \hat{\mathbf{q}}_{kol}^{[j]} \quad (\text{cross-frequency field}), \quad (3.9)$$

$$\phi_{k+l}^{[i]}(\mathbf{x}, f_{k+l}) = \sum_{j=1}^{N_{\text{blk}}} a_{ij}(f_{k+l}) \hat{\mathbf{q}}_{k+l}^{[j]} \quad (\text{bispectral modes}), \quad (3.10)$$

that share a common set expansion coefficients a_{ij} . In the light of equation (2.12), this corresponds to discriminating between the resonantly forced wave component at $\mathcal{O}(\epsilon^2)$ and the product of the two interacting components of $\mathcal{O}(\epsilon)$. Equations (3.9) and (3.10) describe expansions into the spaces spanned by the ensembles of realizations of $\hat{\mathbf{q}}_{kol}$ and $\hat{\mathbf{q}}_{k+l}$, respectively. We will refer to ϕ_{k+l} as *bispectral modes*. Bispectral modes are linear combinations of Fourier modes and can be interpreted as observable physical structures. The multiplicative cross-frequency fields ϕ_{kol} , on the contrary, are maps of phase-alignment between two frequency components that may not directly be observed. A more compact form of equations (3.9) and (3.10) is

$$\phi_{kol}^{[i]} = \hat{\mathbf{Q}}_{kol} \mathbf{a}_i, \quad (3.11)$$

$$\phi_{k+l}^{[i]} = \hat{\mathbf{Q}}_{k+l} \mathbf{a}_i, \quad (3.12)$$

where $\mathbf{a}_i = [a_{i1}(f_{k+l}), a_{i2}(f_{k+l}), \dots, a_{iN_{\text{blk}}}(f_{k+l})]^T$ denotes the i -th vector of expansion coefficients for the (k, l) frequency doublet, and $\hat{\mathbf{Q}}_{kol}, \hat{\mathbf{Q}}_{k+l} \in \mathbb{C}^{M \times N_{\text{blk}}}$ are the data matrices

$$\hat{\mathbf{Q}}_{kol} \equiv \begin{bmatrix} \left| \hat{\mathbf{q}}_{kol}^{[1]} \right\rangle & \left| \hat{\mathbf{q}}_{kol}^{[2]} \right\rangle & \dots & \left| \hat{\mathbf{q}}_{kol}^{[N_{\text{blk}}]} \right\rangle \end{bmatrix}, \quad \hat{\mathbf{Q}}_{k+l} \equiv \begin{bmatrix} \left| \hat{\mathbf{q}}_{k+l}^{[1]} \right\rangle & \left| \hat{\mathbf{q}}_{k+l}^{[2]} \right\rangle & \dots & \left| \hat{\mathbf{q}}_{k+l}^{[N_{\text{blk}}]} \right\rangle \end{bmatrix}. \quad (3.13)$$

The goal of bispectral mode decomposition is to compute modes that optimally represent the data in terms of the integral bispectral density. That is, we seek the set of expansion coefficients \mathbf{a}_1 that maximizes the absolute value of $b(f_k, f_l)$ as defined in equation (3.7). To guarantee boundedness of the expansion, we require the coefficient vector to be a unit vector with $\|\mathbf{a}_1\| = 1$. The optimal \mathbf{a}_1 hence has to satisfy

$$\begin{aligned} \mathbf{a}_1 &= \arg \max_{\|\mathbf{a}\|=1} \left| E \left[\phi_{kol}^{[1]H} \mathbf{W} \phi_{k+l}^{[1]} \right] \right| = \arg \max_{\|\mathbf{a}\|=1} \left| E \left[\mathbf{a}^H \hat{\mathbf{Q}}_{kol}^H \mathbf{W} \hat{\mathbf{Q}}_{k+l} \mathbf{a} \right] \right| \\ &= \arg \max \left| \frac{\mathbf{a}^H E \left[\hat{\mathbf{Q}}_{kol}^H \mathbf{W} \hat{\mathbf{Q}}_{k+l} \right] \mathbf{a}}{\mathbf{a}^H \mathbf{a}} \right| = \arg \max \left| \frac{\mathbf{a}^H \mathbf{B} \mathbf{a}}{\mathbf{a}^H \mathbf{a}} \right|, \end{aligned} \quad (3.14)$$

where we introduced

$$\mathbf{B} = \mathbf{B}(\mathbf{x}, \mathbf{x}', f_k, f_l) \equiv \frac{1}{N_{\text{blk}}} \hat{\mathbf{Q}}_{\text{col}}^H \mathbf{W} \hat{\mathbf{Q}}_{k+l} \quad (3.15)$$

as the weighted (auto-) bispectral density matrix. Here, ‘auto’ implies that three frequency components of the same state \mathbf{q} are involved. Consistent with the nomenclature for higher-order statistics of time-signals, we reserve the term cross-bispectrum for third-order statistics such as $S_{qqr}(f_1, f_2)$ or $S_{qrs}(f_1, f_2)$ that involve two or three different fields. In the context of multidimensional data, spatial cross-correlation between any two locations \mathbf{x} and \mathbf{x}' is always implied. The final expression in equation (3.14) corresponds to finding the complex vector $\mathbf{a} \in \mathbb{C}^{N_{\text{blk}} \times 1}$ that maximizes the absolute value of the Rayleigh quotient of the complex, non-Hermitian, square matrix $\mathbf{B} \in \mathbb{C}^{N_{\text{blk}} \times N_{\text{blk}}}$. This problem is directly related to the numerical range, or field of values, which is defined as the set of all Rayleigh quotients of a matrix,

$$F(\mathbf{B}) = \left\{ \frac{\mathbf{a}^H \mathbf{B} \mathbf{a}}{\mathbf{a}^H \mathbf{a}} : \mathbf{a} \in \mathbb{C}^{N_{\text{blk}} \times 1}, \mathbf{a} \neq \mathbf{0} \right\}. \quad (3.16)$$

The largest absolute value the numerical range can attain defines the numerical radius

$$r(\mathbf{B}) = \max \{ |\lambda| : \lambda \in F(\mathbf{B}) \}. \quad (3.17)$$

Therefore, the maximization problem (3.14) is equivalent to finding the vector \mathbf{a}_1 associated with the numerical radius of \mathbf{B} ,

$$r(\mathbf{B}) = \max \left| \frac{\mathbf{a}_1^H \mathbf{B} \mathbf{a}_1}{\mathbf{a}_1^H \mathbf{a}_1} \right|.$$

Geometrically, the numerical radius can be interpreted as the radius of the smallest circle about the origin that contains the field of values. It can be shown (see, e.g., Horn & Johnson 1991; Watson 1996) that the numerical radius corresponds to the largest eigenvalue λ_{\max} that the Hermitian matrix

$$\mathbf{H}(\theta) = \frac{1}{2} (\mathbf{e}^{i\theta} \mathbf{B} + \mathbf{e}^{-i\theta} \mathbf{B}^H) \quad (3.18)$$

can attain for some angle $0 \leq \theta < 2\pi$, i.e.,

$$r(\mathbf{B}) = \max_{0 \leq \theta < 2\pi} \lambda_{\max}(\mathbf{H}(\theta)). \quad (3.19)$$

Denote by θ_1 the angle for which expression (3.19) assumes its maximum value and by \mathbf{a}_1 the leading eigenvector such that

$$\mathbf{H}(\theta_1) \mathbf{a}_1 = \lambda_1 \mathbf{a}_1.$$

Then $\lambda_1 = \lambda_{\max}(\mathbf{H}(\theta_1))$ is the numerical radius and \mathbf{a}_1 maximizes the absolute value of the Rayleigh quotient of \mathbf{B} , i.e.,

$$r(\mathbf{B}) = \lambda_1 = \left| \frac{\mathbf{a}_1^H \mathbf{B} \mathbf{a}_1}{\mathbf{a}_1^H \mathbf{a}_1} \right|.$$

To distinguish λ_1 from the traditional definition of the bispectrum for time-series, we will refer to

$$\lambda_1(f_k, f_l) \quad (\text{complex mode bispectrum}) \quad (3.20)$$

as the *complex mode bispectrum*. It is tempting to approximate the eigenpair $(\lambda_1, \mathbf{a}_1)$ by solving equation (3.19) over a discretized interval $\theta \in (0, 2\pi]$ to find θ_1 . Instead of this

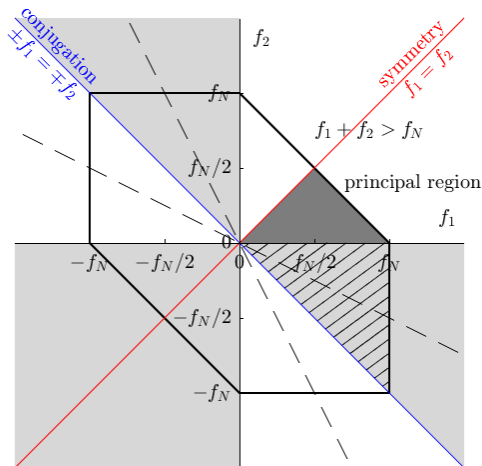


FIGURE 1. The 12 symmetry regions of the bispectrum. The dark shaded triangle indicates the principal region of non-redundant information of the auto-bispectrum. White regions inside the hexagon contain the same information as the principal region. Light gray shading indicates complex conjugation. The principal region corresponds to sum interactions with $f_3 = f_1 + f_2$ and the hatched segment to difference interactions with $f_3 = f_1 - f_2$.

brute-force approach, we employ the much more elegant and efficient algorithm by He & Watson (1997). The algorithm is reproduced, with minor modifications, in appendix A.

3.1. Symmetries and principal region of the bispectrum

3.1.1. Temporal homogeneity

The Nyquist frequency limit restricts the discrete bispectrum to the hexagonal region outlined in figure 1. Within this region, it suffices to compute the bispectrum within the principal region $0 \leq f_2 \leq f_N/2$ and $f_2 \leq f_1 \leq f_N - f_2$. The remaining 11 regions carry the same information as the principal region and its complex conjugate. This symmetry of the bispectrum results the symmetry of the discrete-time Fourier transform for stationary signals, which translates into, among others, the following symmetries for the bispectrum: $S_{qqq}(f_1, f_2) = S_{qqq}(f_2, f_1) = S_{qqq}^*(-f_1, f_2) = S_{qqq}^*(-f_2, f_1 + f_2) = S_{qqq}^*(-f_1, f_1 + f_2)$. In particular, this implies that sum and difference interactions in equation (2.23a) do not have to be considered separately. All symmetry relations can be inferred from the schematic in figure 1.

3.1.2. Spatial homogeneity

Taking spatial homogeneity into account is beneficial not only in terms of computational efficiency, but also for convergence of the spectral estimate and interpretability. Spatial symmetries, such as periodicity, are accounted for through discrete-space Fourier transformation in the corresponding directions. The transformation to wavenumber space permits the identification of the phase coupling between different spatial scales in the same way as the temporal transform for time scales. Take as an example data that are invariant under translation in the x direction. Analogous to the treatment of time for a stationary random signal, we may assume that the spatial bicoherence in x only depends on the relative distances $x - \xi_1$ and $x - \xi_2$. We may hence define the spatio-temporal bicoherence as

$$R_{qqq}(\xi_1, \xi_2, \tau_1, \tau_2) = E[q(x, t), q(x - \xi_1, t - \tau_1), q(x - \xi_1, t - \tau_2)]. \quad (3.21)$$

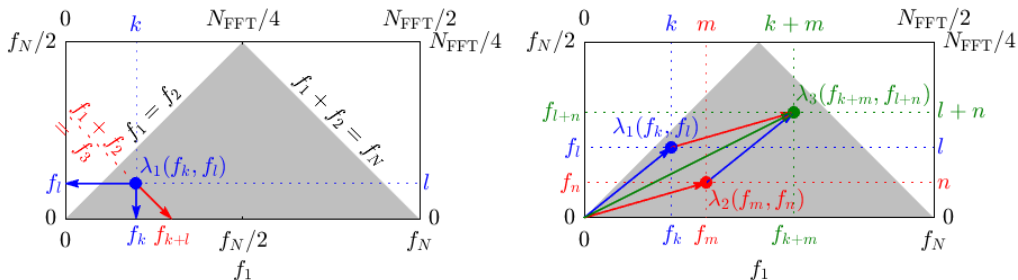


FIGURE 2. Frequency triads in the principal region of the mode bispectrum. Left: a local maximum $\lambda_1(f_k, f_l)$ indicates phase-coupling between the components of the triad $\{f_k, f_l, f_{k+l}\}$ due to quadratic nonlinearity. Harmonics and the mean flow distortion (not shown) are generated by self-interactions like $\{f_k, f_k, f_{2k}\}$ and $\{f_k, f_{-k}, 0\}$, respectively. Right: the sum components generated by two triads, $\{f_k, f_l, f_{k+l}\}$ and $\{f_m, f_n, f_{m+n}\}$, can interact to generate a new wave component $\{f_{k+m}, f_{l+n}\}$.

The spatio-temporal Fourier transform of $R_{qqq}(\xi_1, \xi_2, \tau_1, \tau_2)$ yields the spatio-temporal bispectrum

$$S_{qqq}(k_1, k_2, f_1, f_2) = \lim_{T \rightarrow \infty} \frac{1}{T} E[\hat{q}(k_1, f_1)^* \hat{q}(k_2, f_2)^* \hat{q}(k_1 + k_2, f_1 + f_2)], \quad (3.22)$$

where we denote as k the x -component of the wavenumber vector. Equation (3.22) is analogous to Yamada *et al.* (2010)'s definition of the two-dimensional bispectrum. Equation (3.22) implies that the bispectrum is to be computed for each wavenumber doublet $\{k_1, k_2\}$ individually. Triadically-consistent wavenumber triplets $\{k_1, k_2, k_1 + k_2\}$ are referred to as spatial triads. For the example of three-dimensional data that are translationally invariant in the x -direction, the BMD is therefore computed from the discrete-space discrete-time transformed data $\hat{\mathbf{q}}(\mathbf{z}, k, f)$, where by $\mathbf{z} = [y, z]^T$ we denote the position vector of the remaining inhomogeneous directions. Accordingly, the bispectral density matrix specializes to

$$\mathbf{B}(\mathbf{x}, \mathbf{x}', f_k, f_l) \rightarrow \mathbf{B}(\mathbf{z}, \mathbf{z}', k_i, k_j, f_k, f_l), \quad (3.23)$$

and is computed from $\hat{\mathbf{q}}(\mathbf{z}, k_i, f_k)$, $\hat{\mathbf{q}}(\mathbf{z}, k_j, f_l)$, and $\hat{\mathbf{q}}(\mathbf{z}, k_{i+j}, f_{k+l})$. The resulting BMD modes are two-dimensional and the spatio-temporal mode bispectrum is defined in the four-dimensional wavenumber-wavenumber-frequency-frequency domain. For doubly-homogeneous flows such as pipe or Couette flows, the BMD is computed for all combinations between two wavenumbers and frequency and the resulting modes are one-dimensional.

3.1.3. Principal region of the bispectrum

Figure 2 shows a schematic of the principal region of the mode bispectrum. All other regions contain redundant information or lie outside of the Nyquist limit. It hence suffices to plot this region. For brevity, we will often use integer frequency index doublets (k, l) , or triplets $(k, l, k + l)$, instead of frequency doublets $\{f_k, f_l\}$, or triplets $\{f_k, f_l, f_{k+l}\}$, to represent triads. Figure 2(b) illustrates the generation of new wave components through triad interactions. In the examples discussed in §4, we will observe that this mechanism, starting from the self-interaction of a self-excited or forced fundamental mode, often leads to a distinct grid pattern of the bispectrum.

Case	Variables	N_x	N_y, N_r	N_z, N_θ	N_t	Δt	N_{FFT}	N_{ovlp}	N_{blk}	tol
Cylinder DNS	u, v	250	125	1	4096	0.06	1024	512	7	10^{-8}
Plate PIV	u, v	120	69	1	$2.5 \cdot 10^4$	$0.002s$	5000	0	50	10^{-8}
Jet LES	p	219	42	128	$1 \cdot 10^4$	0.2	256	128	77	10^{-15}

TABLE 1. Parameters of the example databases and spectral estimation parameters. The DNS and LES data are non-dimensionalized by the cylinder diameter and freestream velocity, and the jet diameter and jet velocity, respectively. The PIV data are given in SI units. tol is the tolerance used by the algorithm presented in appendix A.

4. Examples

Since the mode bispectrum is complex, we visualize its modulus, the (*magnitude mode bispectrum* $|\lambda_1(f_k, f_l)|$), and argument, the (*phase mode bispectrum* $\arg(\lambda_1(f_k, f_l))$), separately. We further define the *summed mode spectrum* as

$$A_1(f) \equiv \frac{1}{N(f)} \sum_{f=f_1+f_2} |\lambda_1(f_1, f_2)| \quad (\text{summed mode spectrum}), \quad (4.1)$$

where $N(f)$ is the number of frequency doublets $\{f_1, f_2\}$ that contribute to any frequency $f = f_1 + f_2$, that is, the number of terms in the sum. Graphically, this corresponds to summing λ_1 along diagonals of slope -1 , corresponding to lines of constant frequency, in the principal region of the mode bispectrum. Take as an example is the red line of constant frequency f_3 in figure 2. Peaks in the summed mode spectrum indicate that the corresponding frequencies are involved in quadratic nonlinear interactions, but without discriminating between the contributing triads.

Equations (3.14) implies that the mode bispectrum derives from the spatial integration of the Hadamard product

$$\psi_{k,l}(\mathbf{x}, f_k, f_l) \equiv |\phi_{k+ol} \circ \phi_{k+l}| \quad (\text{interaction map}). \quad (4.2)$$

We hence may interpret the field $\psi_{k,l}$ as an *interaction map* that quantifies the average local bicoherence between three frequency components f_l , f_k , and $f_k + f_l$. The interaction map augments the bispectral modes in that it indicates regions of activity of triadic interaction.

In what follows, we conduct BMD analyses of the three representative nonlinear flows summarized in table 1. The goal of this section is to demonstrate different aspects of BMD using different data—an exhaustive discussion of the nonlinear flow physics of each of these flows is beyond the scope of this work. The dimensionless frequency used for the numerical data corresponds to the Stouhal number, but we retain the symbol f for readability. The trade-offs involved in choosing the spectral estimation parameters N_{FFT} and N_{ovlp} and the windowing function are similar to those for SPOD. The reader is referred to Schmidt & Colonius (2020) for best practices that in large parts translate to BMD.

4.1. Cylinder flow

The flow over a cylinder at a Reynolds number, based on the cylinder diameter and the free-stream velocity, of $Re = 500$ is a canonical laminar, planar flow that exhibits well-understood nonlinear dynamics (Williamson 1996). The immersed-boundary solver by Goza & Colonius (2017) was used to solve the incompressible Navier-Stokes equations for the state vector $\mathbf{q} = [u, v]^T$, consisting of the streamwise and transverse velocity

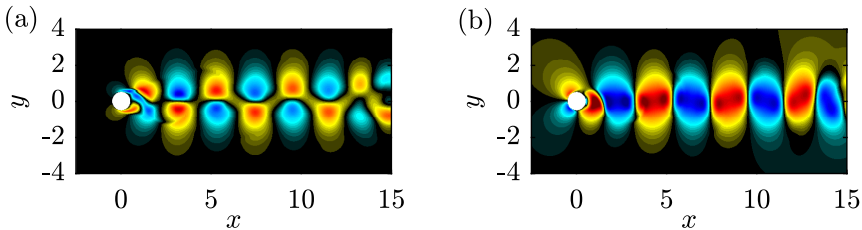


FIGURE 3. Instantaneous fluctuating flow field behind a cylinder at $Re = 500$: (a) streamwise velocity; (b) transverse velocity. Colormap is saturated at $\pm 75\%$ of the free-stream velocity.

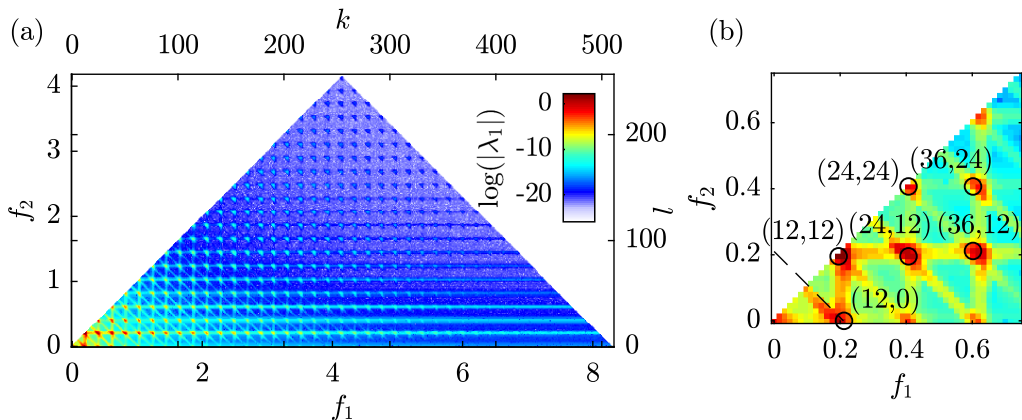


FIGURE 4. (Magnitude) mode bispectrum for cylinder flow at $Re = 500$: (a) mode bispectrum for $N_{\text{FFT}} = 1024$; (b) magnification of the bottom-left corner. The fundamental vortex-shedding frequency $f_0 = 0.21$ corresponds to frequency index 12. A cascade of triads (o) that originates from the fundamental instability and the diagonal line of constant frequency f_0 (---) are marked in (b).

components. Prior to saving the data, the simulation was run for multiple flow-through times to guarantee that the database reported in table 1 represents the limit-cycle solution. The instantaneous flow field is visualized in figure 3.

Figure 4(a) shows the mode bispectrum and figure 4(b) a magnification of the low-frequency portion. The most striking feature is a distinct grid pattern with local maxima at its nodes. These local maxima are the footprint of a cascade of triads that is generated through the mechanism illustrated in figure 2(b). A closer inspection of figure 4(b) reveals that the global maximum of the mode bispectrum occurs for the index doublet $(k, l) = (12, 12)$, that is, the triad $(k, l, k + l) = (12, 12, 24)$, or $\{f_1, f_2, f_1 + f_2\} = \{0.21, 0.21, 0.42\}$, in terms of frequency. It corresponds to the self-interaction of the fundamental instability with $f_0 = 0.21$. This interactions generates the first harmonic with twice the fundamental frequency, $2f_0 = 0.42$. The horizontal, vertical and diagonal bands in the mode bispectrum are a typical phenomenon in higher-order statistical analysis. We speculate that they partially originate from leakage of high-energy wave components into neighboring frequencies. Take as an example the band along the diagonal corresponding to a constant frequency of $f_1 + f_2 = f_0 = 0.21$. Clearly, this band is associated with the fundamental instability. It attains it maximum on the f_1 -axis at $(12, 0)$ and it is observed despite the fact that bluff-body vortex shedding is a self-excited instability mechanism, as opposed to the result of triadic wave interaction. Interestingly, we may leverage this observation to investigate and visualize the fundamental instability.

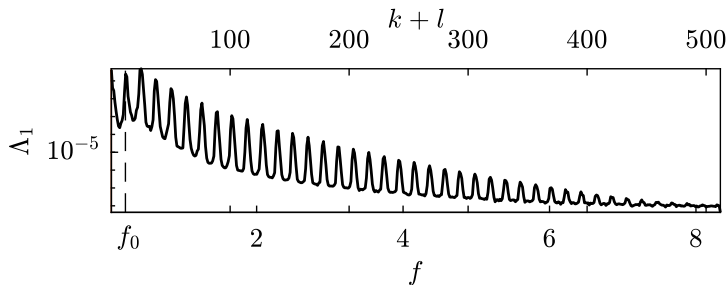


FIGURE 5. Summed mode spectrum for cylinder flow at $Re = 500$. $f_0 = 0.21$ ($k + l = 12$) is the fundamental vortex-shedding frequency.

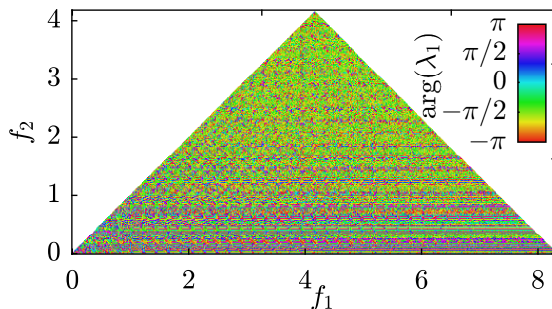


FIGURE 6. Phase mode bispectrum for cylinder flow at $Re = 500$.

The summed mode bispectrum $\Lambda_1(f)$, i.e., the average bispectral density of all frequencies f_1 and f_2 that sum to any given frequency f , is presented in figure 5. A number of peaks clearly identify the fundamental shedding frequency and its higher harmonics. As a function of frequency only, the summed mode bispectrum can directly be compared to power spectra or the SPOD eigenvalue spectrum. It comes to no surprise that the summed mode bispectrum attains its maximum at the frequency of the self-interaction of the fundamental instability.

In figure 6, we report, for completeness, the phase mode bispectrum associated with the magnitude mode bispectrum previously shown in figure 4(a). We do not physically interpret the phase mode bispectrum but would like to emphasize that the phase information it contains may play an important part in low-order models that include quadratic interactions between modes.

The spatial structures of the bispectral modes associated with the cascade of triads previously marked by circles in figure 4(b), are shown in figure 7. The solid and dotted arrows indicate the sum interactions of the k -th and l -th frequency components, respectively, that generate the $k + l$ -th component. The cascade starts with the fundamental mode ϕ_{12+0} . Its self-interaction generates mode ϕ_{12+12} , which in turn partakes in the generation of modes ϕ_{24+12} and ϕ_{24+24} , and so on. The spatial structures of the modes reveals that each interaction yields new wavenumber components in the streamwise and/or transverse directions.

The self-interaction of the fundamental is investigated in more detail in figure 8. The u - and v -components of the corresponding bispectral mode and cross-frequency field are reported in the upper and lower row, respectively. Following the definition in equation (4.2), the entry-wise product of the bispectral mode and the cross-frequency field yields the interaction map shown in figure 8(b,e). The main observations is that the

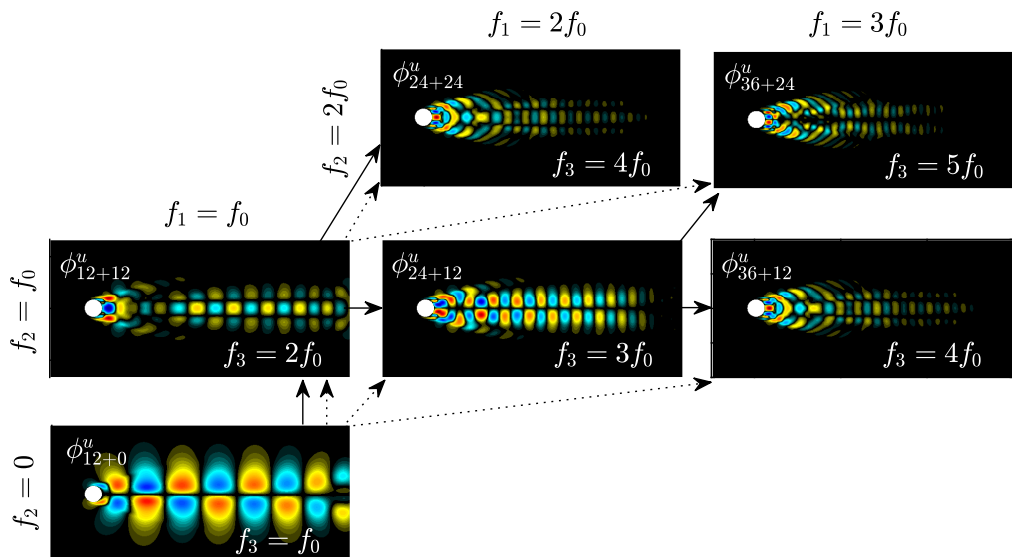


FIGURE 7. Bispectral modes forming a cascade of triads, marked in figure 4, starting from the fundamental instability at f_0 (bottom-left). Arrows indicate the triadic interactions (\rightarrow : k -component, \dashrightarrow : l -component). The real part of the streamwise velocity component is shown.

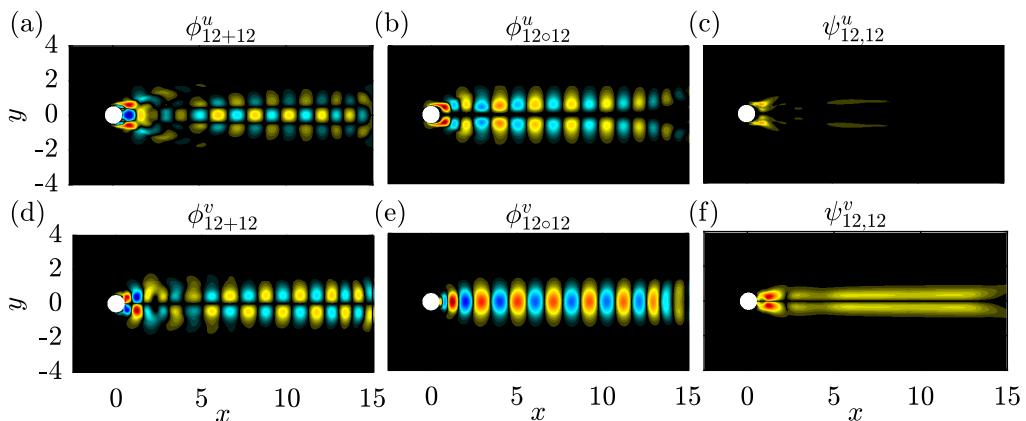


FIGURE 8. Self-interaction of the fundamental mode: (a,d) bispectral mode; (b,e) cross-frequency field; (c,f) interaction map. Top and bottom rows show the u and v components, respectively. False colors of modes are saturated at maximum absolute value. False colors of interaction maps are identical to allow for comparison. The real part of the bispectral modes is shown in (a,b,d,e).

interaction is the strongest in the wake region shortly downstream of the cylinder. The transverse component furthermore attains a larger maximum value than the streamwise component and is less spatially confined. A connection to the sensitivity regions identified experimentally by Strykowski & Sreenivasan (1990), and predicted based on structural stability analysis by Giannetti & Luchini (2007), remains speculative.

4.2. Massively-separated flow behind flat plate at high angle of attack

The second example is that of PIV data of massively-separated flow behind flat plate at high angle of attack. A total of 50 independent measurements consisting of 5000

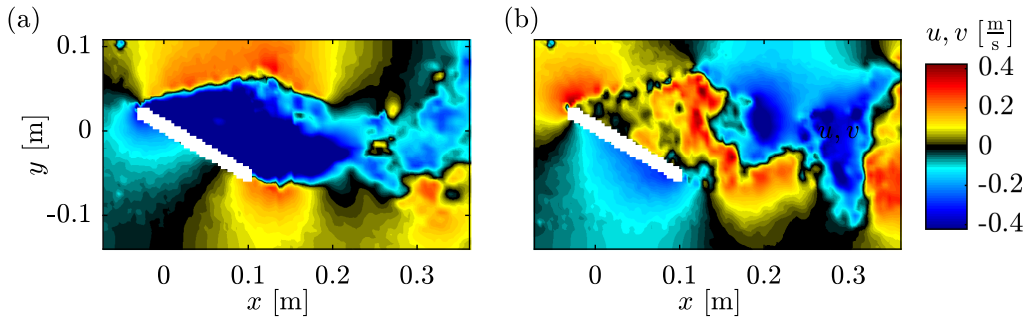


FIGURE 9. Instantaneous PIV flow field of massively-separated flow behind a flat plate: (a) streamwise fluctuating velocity; (b) transverse fluctuating velocity. (Data courtesy of K. Mulleners, EPFL.)

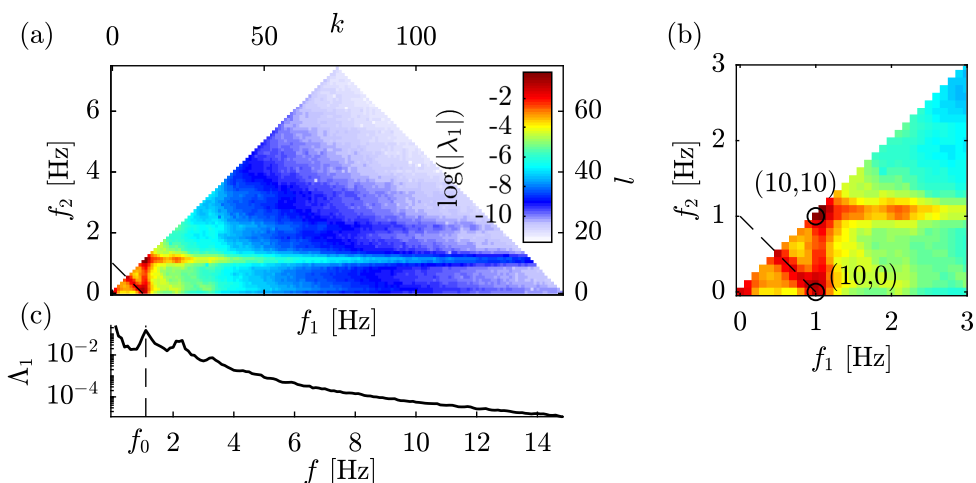


FIGURE 10. Spectra of PIV data of massively-separated flow behind plate: (a) mode bispectrum for $N_{\text{FFT}} = 5000$; (b) magnification of the bottom-left corner; (c) summed mode spectrum. The fundamental vortex-shedding frequency is $f_0 = 1.0\text{ Hz}$ (frequency index 10) is marked by dashed lines (---) in (a,b,c). The global maximum of the mode bispectrum occurs for the self-interaction triad (10, 10) of the fundamental instability.

snapshots each is used. Unlike the cylinder flow simulation data, these data are subject to measurement noise and stochasticity, and exhibit much richer dynamics. This becomes apparent from the instantaneous flow field visualization in figure 9.

The magnitude and summed mode bispectra are shown in figure 10. Similar to figures 4 and 5 for cylinder flow, the mode and summed mode bispectra unveil the signature of bluff-body vortex shedding with the self-interaction triad of the fundamental instability at its center.

As before, we analyze the fundamental self-interaction triad in more detail by inspecting the corresponding bispectral modes, cross-frequency fields and interaction maps. This is done in figure 11. The fundamental vortex shedding mode shown in figure 11(a,b) becomes symmetric at a short distance downstream from the plate. The mode generated by the self-interaction of the fundamental, mode (10, 10), is shown in figure 11(g,h). From inspecting and comparing the interaction maps shown in figure 11(k,l), we conclude that the triadic interaction takes place predominantly in the transverse velocity component and in the bottom shear layer. For both the cylinder flow and the

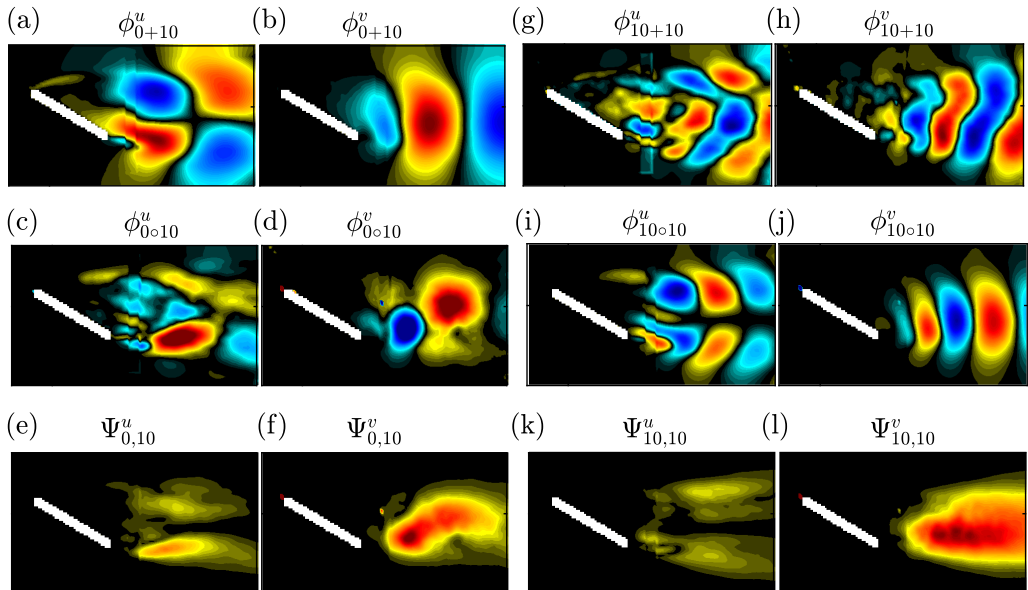


FIGURE 11. Streamwise and transverse components of modes of PIV data of massively-separated flow behind plate: (a-f) fundamental instability; (g-l) self-interaction of fundamental instability. Top, middle and bottom rows show bispectral modes, cross-frequency fields, and interactions maps, respectively. The real part of the bispectral modes is shown in (a-d,g-j). The vertical bar particularly visible in (c,g) is an artifact of two overlapping PIV windows.

massively-separated plate, we confirmed that the fundamental modes, (12,0) and (10,0), respectively, correspond to the overall most energetic large-scale coherent structures as identified by SPOD. In fact, the fundamental bispectral modes shown in figures 7 (bottom-left) and 11(a,b) are almost indistinguishable from the most energetic SPOD modes (not shown). Note that the structures of the leading modes are clearly identified as symmetric and anti-symmetric wave trains, that is despite the stochastic and nature of the data. Comparing the modes with those obtained for laminar cylinder flow suggests that the laminar bluff-body dynamics prevail in the turbulent regime, i.e., at higher Reynolds numbers. The actual shape of the obstacle seems to be secondary. Similar observations have been made by Rigas *et al.* (2014).

4.3. Jet at $Re = 3600$

The example of an initially laminar jet at a moderate Reynolds number of $Re = 3600$ is chosen to demonstrate the treatment of flows with homogeneous directions, here the azimuthal direction in a cylindrically symmetric domain. The large eddy simulation was conducted by Dr. G. A. Brès using the numerical framework discussed in Brès & Lele (2019). The original data was computed on an unstructured grid. The database used here was later interpolated onto a cylindrical grid with coordinates $\mathbf{x} = [x, r, \theta]^T$, where r and θ are the radial and azimuthal coordinates, respectively. We may exploit the cylindrical symmetry of the jet by decomposing the flow field into azimuthal Fourier modes

$$\tilde{\mathbf{q}}(x, r, m, t) = \sum_{j=0}^{N_\theta-1} \mathbf{q}(x, r, \theta_{j+1}, t) e^{-im}, \quad m = 0, \dots, N_\theta - 1 \quad (4.3)$$

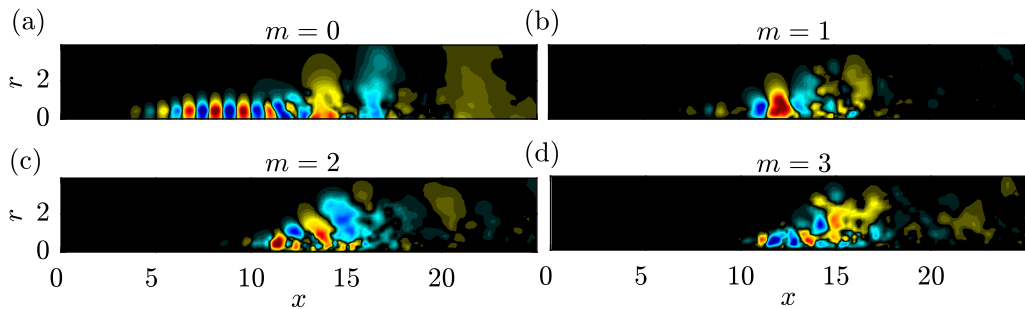


FIGURE 12. Instantaneous pressure fields of the leading azimuthal wavenumber components of the transitional round jet: (a) $m = 0$; (b) $m = 1$; (c) $m = 2$; (d) $m = 3$. False colors are saturated at maximum absolute value of each component. For $m > 0$, the real part of the pressure field is shown.

of azimuthal wavenumber m . Following the discussion in §3.1.2, we consider azimuthal triads which we denote by triplets $\llbracket m_1, m_2, m_3 \rrbracket$, where $m_3 = m_1 + m_2$. We denote by $\llbracket \cdot \rrbracket$ azimuthal wavenumber multiplets, to avoid confusion. Since the jet has no preferred sense of rotation, the azimuthal wavenumber spectrum is expected to be symmetric and it suffices to consider positive azimuthal wavenumbers $m \geq 0$. In the light of rotational symmetry, equation (3.23) specializes as

$$\mathbf{B} \left(\begin{bmatrix} x \\ r \\ \theta \end{bmatrix}, \begin{bmatrix} x' \\ r' \\ \theta' \end{bmatrix}, f_k, f_l \right) \rightarrow \mathbf{B} \left(\begin{bmatrix} x \\ r \end{bmatrix}, \begin{bmatrix} x' \\ r' \end{bmatrix}, m_i, m_j, f_k, f_l \right). \quad (4.4)$$

In the following, we will conduct a bispectral mode analysis on the fluctuating pressure field and restrict our attention, for brevity, to azimuthal wavenumber combinations with $m_3 \leq 3$.

The instantaneous fluctuating pressure fields of the first four azimuthal wavenumber components are shown in figure 12. From figure 12(a), it can be seen that the annular shear-layer supports a symmetric Kelvin-Helmholtz instability that breaks down into turbulence at $x \approx 12$. Comparison with figure 12(b-d) suggests that this breakdown is three-dimensional and leads energy transfer to higher azimuthal wavenumber components. It is this interaction across azimuthal wavenumbers that we study using BMD in the following.

We will not investigate the modes in detail, but instead focus on the mode bispectra for the six principle triplets with $m_3 \leq 3$ shown in figure 13. Maxima in these mode bispectra evidence the presence of azimuthal triads. Given that the jet dynamics are in large parts dominated by the symmetric Kelvin-Helmholtz shear layer roll-up, it comes to no surprise that the fundamental self-interaction occurring for $\llbracket 0, 0, 0 \rrbracket$, $\{f_0, f_0, 2f_0\}$, marked by (o) in figure 13(a), is associated with the global maximum of the bispectral density. The local maxima observed in 13(b-f) suggest that azimuthal wavenumber triads at low frequencies cascade energy to higher and higher azimuthal wavenumbers. For the triplets $\llbracket 0, 0, 1 \rrbracket$ and $\llbracket 1, 1, 2 \rrbracket$ shown in figure 13(b) and 13(c), respectively, this interaction takes place at frequencies $\{\frac{1}{2}f_0, \frac{1}{2}f_0, f_0\}$ and $\{f_0, \frac{1}{2}f_0, \frac{3}{2}f_0\}$, i.e., it involves subharmonic frequencies like $\frac{1}{2}f_0$ and leads to the generation of the ultraharmonic frequency components like $\frac{3}{2}f_0$.

The summed mode spectra for the same azimuthal wavenumber triplets are compared in figure 14. The summed mode spectrum for the $(0, 0, 0)$ interaction has a significantly higher base-level than the other spectra and shows peaks at the fundamental frequency and three higher harmonics. The most prominent peak is observed for the first harmonic

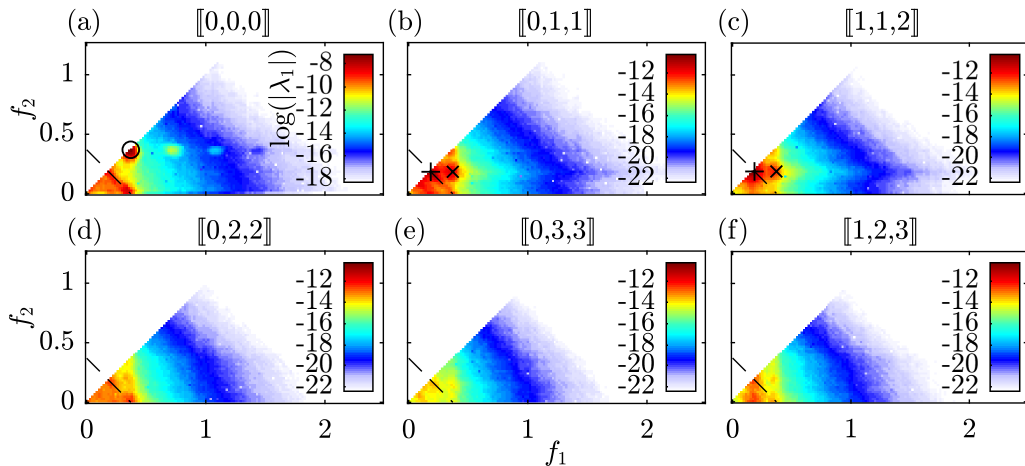


FIGURE 13. Mode bispectra for the interaction of different azimuthal wavenumber components of the transitional jet: (a) self-interaction of $m = 0$; (b) interaction of $m = 1$ and 2; (c) self-interaction of $m = 1$; (d) interaction of $m = 0$ and 2; (e) interaction of $m = 0$ and 3; (f) interaction of $m = 1$ and 2. Azimuthal triads are denoted by triplets $[[m_1, m_2, m_3]]$. Dashed lines (---) mark the diagonal of constant frequency f_0 . False color ranges in (b-f) are identical and significantly lower than for $[[0, 0, 0]]$. The fundamental self-interaction frequency triad $\{f_0, f_0, 2f_0\}$ is marked by ‘o’ in (a), and the triads $\{\frac{1}{2}f_0, \frac{1}{2}f_0, f_0\}$ and $\{f_0, \frac{1}{2}f_0, \frac{3}{2}f_0\}$ as ‘+’ and ‘x’, respectively, in (b,c).

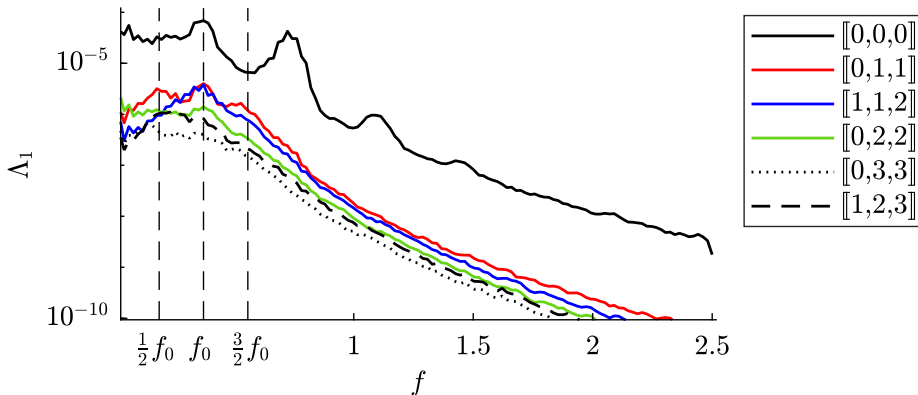


FIGURE 14. Summed mode spectra for the interaction of different azimuthal wavenumber components of the transitional jet. Triplets $[[m_1, m_2, m_3]]$ denote azimuthal triads.

at $f = 2f_0$. For $[[0, 1, 1]]$, peaks on right and left side of the fundamental frequency indicate the presence of the ultraharmonic and the subharmonic frequency components, $\frac{3}{2}f_0$ and $\frac{1}{2}f_0$, respectively.

5. Summary and outlook

Bispectral mode decomposition was introduced as a means of educing coherent structures associated with triad wave interactions from flow data. The decomposition was applied to three experimental and numerical flow databases that represent the laminar, transitional and turbulent regimes. Quadratically interacting frequency components are identified as maxima in the mode bispectrum and the corresponding bispectral modes

reveal the flow structures that are generated through the interaction. Two additional quantities were proposed to aid the analysis: interaction maps identify regions of activity of triadic interaction, and the summed mode bispectrum is a compact representation of the mode bispectrum. The example of a radially symmetric jet was investigated specifically to illustrate the treatment of homogenous directions.

There are several possible extensions and applications of BMD. For example, the present method can readily be extended to the analysis of four-wave resonances based on the trispectrum, $S_{qqqq}(f_1, f_2, f_3)$. Four-wave resonances are a common phenomenon in water waves (Hammack & Henderson 1993; Janssen 2003). The trispectrum can be defined both in terms of the fourth-order momentum, or the fourth-order cumulant. This distinction was not necessary for BMD, as moments and cumulants for third- and lower-orders statistics coincide. The cumulant trispectrum is presumably preferable in this context as it excludes contributions from lower-order moments.

The method proposed here is based on to the maximization problem for the absolute value of the spatio-temporal bispectral density, equation (3.14). It was shown that this problem is directly related to the numerical radius of the bispectral density matrix as defined in equation (3.15). For different applications, the computation of modes with different properties is also of potential of interest. Note that, because the bispectral density matrix is non-Hermitian, the definition of meaningful hierarchy of suboptimal modes, that is inherent to POD, is not obvious.

In this work, we introduced BMD as a means of unveiling and analyzing triadic interactions from flow data. Potential future applications of BMD include reduced-order models. The estimation of nonlinear transfer functions using the cross-bispectrum has previously been explored by Ritz & Powers (1986). Following this idea, quadratic transfer functions obtained from BMD mode bispectra may potentially be used to model intermodal energy transfer in BMD-based reduced-order models.

The Matlab code used to compute the results is freely available. Two versions are provided. The first version solves the BMD based on the auto-bispectral density $S_{qqq}(f_1, f_2)$, as introduced in §3. The second variant solves the corresponding problem for the cross-bispectral density $S_{qrs}(f_1, f_2) = \lim_{T \rightarrow \infty} \frac{1}{T} E[\hat{q}(f_1)\hat{r}(f_2)\hat{s}(f_1 + f_2)^*]$. This second variant was used to investigate azimuthal wavenumber interactions in §4.3. Other applications of this version include quadratic phase coupling between different flow quantities or external fields.

Acknowledgements I would like to thank Tim Colonius for pointing me to higher-order spectra and Aaron Towne, Peter Schmid, Georgios Rigas and Tim Colonius for many helpful discussions. I gratefully acknowledge Karen Mulleners for providing the PIV data, Guillaume Brès for the LES data, Andres Goza for helping with the DNS, and Tianyi Chu for feedback on the initial manuscript.

Appendix A. Computation of $\mathbf{a}_1 = \arg \max_{\|\mathbf{a}\|=1} |\mathbf{a}^* \mathbf{B} \mathbf{a}|$

A slightly modified version of the algorithm for the computation of the numerical radius by He & Watson (1997) is used. He and Watson's algorithm requires two nested iterations. The first, or so-called simple iteration (Watson 1996), converges to a local solution of equation (3.19). A tolerance of $tol = 10^{-8}$ was found to be a good compromise between accuracy and compute time for both iterations. The number of iterations was limited to $k = 300$.

Algorithm 1 (Watson's Simple Iteration)

Data: \mathbf{B} , tol and \mathbf{a}_0 , a complex vector as initial guess.

Result: \mathbf{a} and w , a local solution of equation (3.19).

for $k = 1, 2, \dots$ **do**

 Set $w_{k-1} = \mathbf{a}_{k-1}^H \mathbf{B} \mathbf{a}_{k-1}$.

 Define \mathbf{a}_k by

$$\mathbf{a}_k = w_{k-1} \mathbf{B}^H \mathbf{a}_{k-1} + w_{k-1}^H \mathbf{B} \mathbf{a}_{k-1}.$$

 Normalize $\mathbf{a}_k \leftarrow \frac{\mathbf{a}_k}{\|\mathbf{a}_k\|}$.

 Return $\mathbf{a} = \mathbf{a}_k$ and $w = \mathbf{a}_k^H \mathbf{B} \mathbf{a}_k$ if $|w_{k-1} - w_{k-2}| < tol$.

end

Building on the simple iteration to find local solutions, the purpose of the main algorithm is to find the global solution. Double precision arithmetic with machine precision $\epsilon = 2^{-52}$ was used to compute the results in §4. If the algorithm did not converge within 500 iterations, it was restarted up to five times with a new random initial guess for \mathbf{a}_0 . This procedure was necessary to ensure that all results are fully converged.

Algorithm 2 (He and Watson's Algorithm)

Data: \mathbf{B} and tol .

Result: $\mathbf{a} \approx \mathbf{a}_1$, $lb \approx r(\mathbf{B})$, ub . lb and ub are a lower bound and an upper bound of $r(\mathbf{B})$, such that $ub - lb \leq tol$.

Set \mathbf{a}_0 to a random complex vector.

Set $lb = 0$ and $ub = \|\mathbf{B}\|_1$, the matrix 1-norm of \mathbf{B} .

while $ub - lb > tol$ **do**

 Use Algorithm 1 with starting vector \mathbf{a}_0 to obtain an updated vector \mathbf{a} .

 Set $lb = \max(lb, |\mathbf{a}^H \mathbf{B} \mathbf{a}|)$.

 Set $\alpha = lb + tol$ and solve generalized eigenvalue problem

$$\mathbf{R}(\alpha) \mathbf{v} = \lambda \mathbf{S} \mathbf{v},$$

 where

$$\mathbf{R}(\alpha) = \begin{bmatrix} 2\alpha \mathbf{I} & -\mathbf{B}^H \\ \mathbf{I} & \mathbf{0} \end{bmatrix}, \quad \mathbf{S} = \begin{bmatrix} \mathbf{B} & \mathbf{0} \\ \mathbf{0} & \mathbf{I} \end{bmatrix},$$

 and \mathbf{I} is the $N_{\text{blk}} \times N_{\text{blk}}$ identity matrix.

if $|\lambda - 1| < \sqrt{\epsilon} \|\mathbf{B}\|_1$ for any λ **then**

 (i.e., there is no eigenvalue on the unit circle)

 Set $ub = lb + tol$ and return \mathbf{a} , lb , and ub .

else

 Set \mathbf{a} equal to the last N_{blk} components of an eigenvector \mathbf{v} corresponding to an eigenvalue on the unit circle.

end

end

REFERENCES

- BAARS, W., TINNEY, C. & POWERS, E. 2010 Pod based spectral higher-order stochastic estimation. In *AIAA Paper 2010-1292*, p. 1292.
- BRÈS, GUILLAUME A & LELE, SANJIVA K 2019 Modelling of jet noise: a perspective from large-eddy simulations. *Philosophical Transactions of the Royal Society A* **377** (2159), 20190081.
- BRILLINGER, DAVID R 1965 An introduction to polyspectra. *The Annals of mathematical statistics* pp. 1351–1374.
- COLLIS, WB, WHITE, PR & HAMMOND, JK 1998 Higher-order spectra: the bispectrum and trispectrum. *Mechanical systems and signal processing* **12** (3), 375–394.
- CORKE, T.C, SHAKIB, F & NAGIB, HM 1991 Mode selection and resonant phase locking in unstable axisymmetric jets. *Journal of Fluid Mechanics* **223**, 253–311.
- CORKE, T. C. & MANGANO, R. A. 1989 Resonant growth of three-dimensional modes in transitioning blasius boundary layers. *Journal of Fluid Mechanics* **209**, 93–150.
- CRAIG, S. A., HUMBLE, R. A., HOFFERTH, J. W. & SARIC, W. S. 2019 Nonlinear behaviour of the mack mode in a hypersonic boundary layer. *Journal of Fluid Mechanics* **872**, 74–99.
- CRAIK, ALEXDD 1971 Non-linear resonant instability in boundary layers. *Journal of Fluid Mechanics* **50** (2), 393–413.
- CRAIK, A. D. D. 1988 *Wave interactions and fluid flows*. Cambridge University Press.
- DEANE, AE, KEVREKIDIS, IG, KARNIADAKIS, G EM & ORSZAG, SA 1991 Low-dimensional models for complex geometry flows: application to grooved channels and circular cylinders. *Physics of Fluids A: Fluid Dynamics* **3** (10), 2337–2354.
- FARRELL, B. F. & IOANNOU, P. J. 2003 Structural stability of turbulent jets. *Journal of the atmospheric sciences* **60** (17), 2101–2118.
- FARRELL, B. F., IOANNOU, P. J., JIMÉNEZ, J., CONSTANTINOU, N. C., LOZANO-DURÁN, A. & NIKOLAIDIS, M.-A. 2016 A statistical state dynamics-based study of the structure and mechanism of large-scale motions in plane poiseuille flow. *Journal of Fluid Mechanics* **809**, 290–315.
- GEE, K. L., ATCHLEY, A. A., FALCO, L. E., SHEPHERD, M. R., UKEILEY, L. S., JANSEN, B. J. & SEINER, J. M. 2010 Bicoherence analysis of model-scale jet noise. *The Journal of the Acoustical Society of America* **128** (5), EL211–EL216.
- GIANNETTI, F. & LUCHINI, P. 2007 Structural sensitivity of the first instability of the cylinder wake. *Journal of Fluid Mechanics* **581**, 167–197.
- GOZA, A. & COLONIUS, T. 2017 A strongly-coupled immersed-boundary formulation for thin elastic structures. *Journal of Computational Physics* **336**, 401–411.
- HAMMACK, J. L. & HENDERSON, D. M. 1993 Resonant interactions among surface water waves. *Annual review of fluid mechanics* **25** (1), 55–97.
- HE, C. & WATSON, G. A. 1997 An algorithm for computing the numerical radius. *IMA Journal of Numerical Analysis* **17** (3), 329–342.
- HERRING, J. R. 1980 Theoretical calculations of turbulent bispectra. *Journal of fluid Mechanics* **97** (1), 193–204.
- HERRING, J. R. & MÉTAIS, O. 1992 Spectral transfer and bispectra for turbulence with passive scalars. *Journal of Fluid Mechanics* **235**, 103–121.
- HORN, R. A. & JOHNSON, C.R 1991 Topics in matrix analysis cambridge university press. *Cambridge, UK*.
- JANSSEN, P. A. E. M. 2003 Nonlinear four-wave interactions and freak waves. *Journal of Physical Oceanography* **33** (4), 863–884.
- KIM, Y. C. & POWERS, E. J. 1979 Digital bispectral analysis and its applications to nonlinear wave interactions. *IEEE transactions on plasma science* **7** (2), 120–131.
- KRAICHNAN, R. H. 1967 Inertial ranges in two-dimensional turbulence. *Physics of Fluids* **10** (7), 1417–1423.
- KRAICHNAN, R. H. 1971 Inertial-range transfer in two-and three-dimensional turbulence. *Journal of Fluid Mechanics* **47** (3), 525–535.
- LUMLEY, J. L. 1970 *Stochastic tools in turbulence*. New York: Academic Press.
- MARSTON, JB, CHINI, GP & TOBIAS, SM 2016 Generalized quasilinear approximation: application to zonal jets. *Physical review letters* **116** (21), 214501.

- McKEON, B. J. 2017 The engine behind (wall) turbulence: perspectives on scale interactions. *Journal of Fluid Mechanics* **817**.
- MOFFATT, H. K. 2014 Note on the triad interactions of homogeneous turbulence. *Journal of Fluid Mechanics* **741**.
- NIKIAS, C. L. & MENDEL, J. M. 1993 Signal processing with higher-order spectra. *IEEE Signal processing magazine* **10** (3), 10–37.
- NIKIAS, C. L. & RAGHUVeer, M. R. 1987 Bispectrum estimation: A digital signal processing framework. *Proceedings of the IEEE* **75** (7), 869–891.
- NOACK, B. R., AFANASIEV, K., MORZYŃSKI, M., TADMOR, G. & THIELE, F. 2003 A hierarchy of low-dimensional models for the transient and post-transient cylinder wake. *Journal of Fluid Mechanics* **497**, 335–363.
- PHILLIPS, O. M. 1960 On the dynamics of unsteady gravity waves of finite amplitude part 1. the elementary interactions. *Journal of Fluid Mechanics* **9** (2), 193–217.
- POPE, S. B. 2000 *Turbulent Flows*, 1st edn. Cambridge University Press.
- RIGAS, G., OXLADE, A. R., MORGANS, A. S. & MORRISON, J. F. 2014 Low-dimensional dynamics of a turbulent axisymmetric wake. *Journal of Fluid Mechanics* **755**.
- RITZ, C. P. & POWERS, E. J. 1986 Estimation of nonlinear transfer functions for fully developed turbulence. *Physica D: Nonlinear Phenomena* **20** (2-3), 320–334.
- ROWLEY, C. W., MEZIĆ, I., BAGHERI, S., SCHLATTER, P. & HENNINGSON, D. S. 2009 Spectral analysis of nonlinear flows. *Journal of fluid mechanics* **641**, 115–127.
- SCHMID, P. J. & HENNINGSON, D. S. 2001 *Stability and Transition in Shear Flows*, 1st edn. Springer-Verlag New York.
- SCHMID, P. J. 2010 Dynamic mode decomposition of numerical and experimental data. *Journal of Fluid Mechanics* **656**, 5–28.
- SCHMIDT, O. T. & COLONIUS, T. 2020 Guide to spectral proper orthogonal decomposition. *AIAA Journal* pp. 1–11.
- SIROVICH, L. 1987 Turbulence and the dynamics of coherent structures. *Quarterly of applied mathematics* **45** (3), 561–571.
- STRYKOWSKI, P. J. & SREENIVASAN, K. R. 1990 On the formation and suppression of vortex shedding at low reynolds numbers. *Journal of Fluid Mechanics* **218**, 71–107.
- THOMAS, V. L., BINH, K., JOVANOVIĆ, M. R., FARRELL, B. F., IOANNOU, P. J. & GAYME, D. F. 2014 Self-sustaining turbulence in a restricted nonlinear model of plane couette flow. *Physics of Fluids* **26** (10), 105112.
- TOWNE, A., SCHMIDT, O. T. & COLONIUS, T. 2018 Spectral proper orthogonal decomposition and its relationship to dynamic mode decomposition and resolvent analysis. *Journal of Fluid Mechanics* **847**, 821867.
- WALEFFE, F. 1992 The nature of triad interactions in homogeneous turbulence. *Physics of Fluids A: Fluid Dynamics* **4** (2), 350–363.
- WATSON, G. A. 1996 Computing the numerical radius. *Linear algebra and its applications* **234**, 163–172.
- WELCH, P. 1967 The use of fast Fourier transform for the estimation of power spectra: a method based on time averaging over short, modified periodograms. *IEEE Transactions on audio and electroacoustics* **15** (2), 70–73.
- WILLIAMSON, C. H. K. 1996 Vortex dynamics in the cylinder wake. *Annual review of fluid mechanics* **28** (1), 477–539.
- YAMADA, T., ITOH, S.-I., INAGAKI, S., NAGASHIMA, Y., SHINOHARA, S., KASUYA, N., TERASAKA, K., KAMATAKI, K., ARAKAWA, H., YAGI, M. & OTHERS 2010 Two-dimensional bispectral analysis of drift wave turbulence in a cylindrical plasma. *Physics of Plasmas* **17** (5), 052313.